

Missing energy signature from invisible decays of dark photons at the CERN SPS

S.N. Gninenko¹, N.V. Krasnikov^{1,2}, M.M. Kirsanov¹, and D.V. Kirpichnikov¹

¹ *Institute for Nuclear Research of the Russian Academy of Sciences, 117312 Moscow, Russia*

² *Joint Institute for Nuclear Research, 141980 Dubna, Russia*

(Dated: December 9, 2024)

The dark photon (A') production through the mixing with the bremsstrahlung photon from the electron scattering off nuclei can be accompanied by the dominant invisible A' decay into dark-sector particles. In this work we discuss the missing energy signature of this process in the experiment NA64 aiming at the search for $A' \rightarrow \text{invisible}$ decays with a high-energy electron beam at the CERN SPS. We show the distinctive distributions of variables that can be used to distinguish the $A' \rightarrow \text{invisible}$ signal from background. The results of the detailed simulation of the detector response for the events with and without A' emission are presented. The efficiency of the signal event selection is estimated. It is used to evaluate the sensitivity of the experiment and show that it allows to probe the still unexplored area of the mixing strength $10^{-6} \lesssim \epsilon \lesssim 10^{-2}$ and masses up to $M_{A'} \lesssim 1$ GeV. The results obtained are compared with the results from other calculations. In the case of the signal observation, a possibility of extraction of the parameters $M_{A'}$ and ϵ by using the missing energy spectrum shape is discussed. We consider as an example the A' with the mass 16.7 MeV and mixing $\epsilon \lesssim 10^{-3}$, which can explain an excess of events recently observed in nuclear transitions of an excited state of ^8Be . We show that if such A' exists its invisible decay can be observed in NA64 within a month of running, while data accumulated during a few months would allow also to determine the ϵ and $M_{A'}$ parameters.

PACS numbers: 14.80.-j, 12.60.-i, 13.20.Cz, 13.35.Hb

I. INTRODUCTION AND MOTIVATION

The origin of dark matter is a great puzzle in the cosmology and particle physics. In recent years, various phenomenological models assumed the existence of a light vector boson, the "dark photon" A' , with a mass $m_{A'} \lesssim 1$ GeV resulting from a spontaneously broken new gauge symmetry $U(1)_D$. The A' couples to the standard model (SM) particles only through the kinetic mixing of dark charge with hypercharge, parametrized by the mixing strength $\epsilon \ll 1$ [1–3]. The A' kinetically mixes with the photon and couples primarily to the electromagnetic current with a strength ϵe , where e is the electromagnetic coupling. The phenomenology of A' , motivated by potential astrophysical signals of dark matter [4], as well as the 3.6σ discrepancy between the SM prediction and measurements of the muon anomalous magnetic dipole moment $g-2$ [5] has been studied in many theoretical and experimental works [4, 6–10].

If the A' is the lightest particle in the dark sector, it will decay dominantly into ordinary particles, e.g. e, μ . However, if there are lighter dark sector states, A' would decay predominantly into such particles resulting in the $A' \rightarrow \text{invisible}$ decay. This will occur assuming that $e_D \gg \epsilon e$, where e_D is the coupling constant of the $U(1)_D$ gauge interaction with light dark matter particles. Such A' , which is nearly "invisible", provides new possibilities to explain various anomalies including the muon $g-2$ problem and is a subject of different

experimental constraints [11–14] and new experimental searches. Interestingly, that both the muon ($g-2$) anomaly [8–10] and a possible evidence for a new boson from Ref.[15], can be explained by the existence of a sub-GeV A' with the couplings $\epsilon \simeq 10^{-3}$, although there is some tension with constraints from the $(g-2)_e$. Such couplings naturally arise from the loop effects of particles that are charged under both the standard model (SM) and dark hypercharge $U(1)$ interactions [3].

One possible way to search for the invisible A' is based on production and detection sub-GeV dark matter in accelerator experiments. The A' s produced in a high intensity beam dump experiment, decay in flight and produce other dark matter particles which can be detected through the scattering of electrons in the detector target [11, 12, 16–18]. The signal event rate depends on the A' couplings to the dark and visible sectors, e_D and ϵe respectively and scaled by $\epsilon^2 e_D^2 / e^2$. Another approach considered in this work and proposed in Refs.[19, 20], is based on the detection of the large missing energy, carried away by the energetic A' produced in the interactions of high-energy electrons in the active beam dump target, see also [11]. The advantage of the second type of experiments is that their sensitivity is roughly proportional to the mixing squared, ϵ^2 , associated with the A' production in the primary reaction and its subsequent prompt invisible decay, while in the former case it is proportional to ϵ^4 , one ϵ^2 coming from the A' production in the beam dump and another ϵ^2 from the cross section of the dark matter particle

interactions in the active detector.

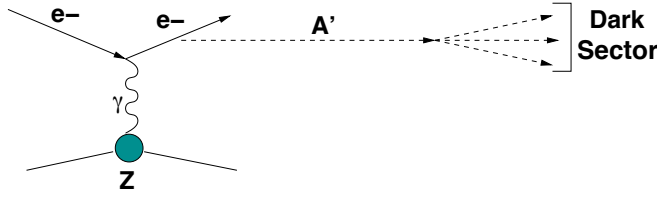


FIG. 1: Diagram contributing to the A' production in the reaction $e^- Z \rightarrow e^- Z A'$, $A' \rightarrow \text{dark sector}$. The produced A' decays invisibly into dark sector particles.

In this work we discuss the fixed-target experiment NA64 at the CERN SPS [19, 20] aiming at the search for $A' \rightarrow \text{invisible}$ decays with a 100 GeV electron beam. Different background sources that could mimic the signal in this experiment were studied in detail in Refs.[19, 20], see also [11]. It has been shown that for the mixing $10^{-6} \lesssim \epsilon \lesssim 10^{-3}$ and masses $M_{A'} \lesssim 1$ GeV the proposed search is essentially background free at least at the level $\lesssim 10^{-12}$ per incident electron. Here, we focus mainly on the A' production rate, experimental signature of the $A' \rightarrow \text{invisible}$ decays, and sensitivity of the experiment. Our goal is two-fold. First, in light of recent disagreements in the literature on the question of the A' yield computations [11], we revisit here the calculations of Ref.[19, 20]. We seek to clarify the apparent disagreements about the numerical factors in the analytic expressions for the A' yield computations. Obtaining a reliable theoretical prediction for the A' yield is essential for the proper interpretation of the obtained experimental results in terms of the possible observation of the A' signal or obtaining a robust exclusion limits in the A' parameter space.

Second, we attempt to provide an estimate of the experimental uncertainties associated with the A' signal calculation required for the sensitivity estimate. While the study of Ref.[11] included some theoretical uncertainties associated with the A' modeling and experimental data used as input for the calculation, no estimate of the errors and factors related to the concrete experimental setup configuration was given. We discuss additional experimental inputs that would be useful to improve the reliability of the calculated sensitivity of the experiment. We extend the analysis of Ref.[20] by simulating the full detector response and taking into account the realistic production and detection efficiency for signal events. Finally, the feasibility of reconstruction of the signal parameters such as the mass and the mixing strength of the A' from the observed shape of the E_{miss} spectrum has been studied for the benchmark values $M_{A'} = 16.7$ MeV and $\epsilon \simeq 10^{-3}$. The hint at the existence of the A' with such properties,

has been recently found by the experiment of Ref. [15]. An observed excess of e^+e^- pairs in nuclear transitions of an excited state of ^8Be could originate from the decay $A' \rightarrow e^+e^-$ with the branching fraction $\simeq 10\%$, while the predominant A' decay mode is $A' \rightarrow \text{invisible}$.

The remainder of our treatment of these issues is organized as follows. Section II outlines the theoretical setup for the A' production in electron- nuclei scattering, observables that are analyzed and the signal simulation. The results of the detector response simulation are reported in Section III. Section IV is dedicated to the discussion of the missing energy signature of the signal events A' yield. The results of the detailed detector response simulation are reported in Section V. In Section VI the expected sensitivity of the search is discussed and compared with the existing calculations obtained by Izaguirre et al. in [11]. We conclude the article with a short summary in Section VII.

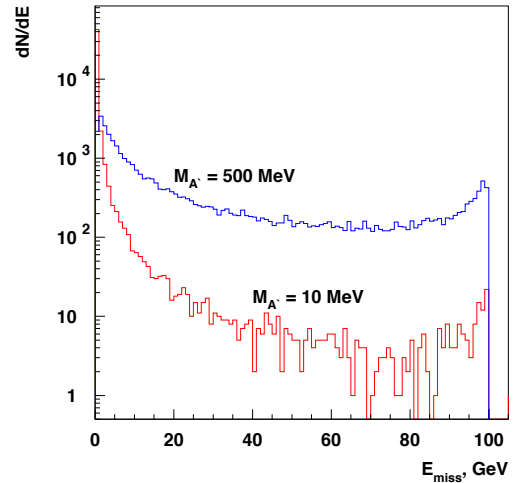


FIG. 2: The A' emission spectrum from 100 GeV electron beam interactions in the Pb target calculated for $m_{A'} = 10$ MeV and $m_{A'} = 500$ MeV. The spectra are normalized to about the same number of events.

II. THE A' PRODUCTION AND SPECTRA

The Lagrangian of the SM is extended by the dark sector in the following way:

$$\mathcal{L} = \mathcal{L}_{SM} - \frac{1}{4}F'_{\mu\nu}F'^{\mu\nu} + \frac{\epsilon}{2}F'_{\mu\nu}F^{\mu\nu} + \frac{m_{A'}^2}{2}A'_\mu A'^\mu + i\bar{\chi}\gamma^\mu\partial_\mu\chi - m_\chi\bar{\chi}\chi - e_D\bar{\chi}\gamma^\mu A'_\mu\chi, \quad (1)$$

where A'_μ is massive vector field of spontaneously broken $U'(1)$ gauge group, $F'_{\mu\nu} = \partial_\mu A'_\nu - \partial_\nu A'_\mu$, and ϵ is parameter of photon-paraphoton kinetic mixing. Here,

we consider as an example the Dirac spinor fields χ which are treated as Dark Matter fermions coupled to A'_μ by dark portal coupling constant g_D . The mixing term $\frac{\epsilon}{2} F'_{\mu\nu} F^{\mu\nu}$ results in the interaction:

$$\mathcal{L}_{int} = \epsilon e A'_\mu J_{em}^\mu \quad (2)$$

of dark photons with the ordinary matter. The decay rates of $A' \rightarrow \bar{\chi}\chi$ and $A' \rightarrow e^-e^+$ are given by

$$\begin{aligned} \Gamma(A' \rightarrow \bar{\chi}\chi) &= \frac{\alpha_D}{3} m_{A'} \left(1 + \frac{2m_\chi^2}{M_{A'}^2}\right) \sqrt{1 - \frac{4m_\chi^2}{M_{A'}^2}}, \\ \Gamma(A' \rightarrow e^-e^+) &= \frac{\alpha_{QED}\epsilon^2}{3} m_{A'} \left(1 + \frac{2m_e^2}{M_{A'}^2}\right) \sqrt{1 - \frac{4m_e^2}{M_{A'}^2}}. \end{aligned} \quad (3)$$

We suppose that dark matter invisible decay mode is predominant, i.e. $\Gamma(A' \rightarrow \bar{\chi}\chi)/\Gamma_{tot} \simeq 1$. This means that the A' lepton decay channel is suppressed, $\Gamma(A' \rightarrow \bar{\chi}\chi) \gg \Gamma(A' \rightarrow e^-e^+)$.

We consider the high-energy electron beam absorption in the active target as a source of A' s. In this case dark photons can be produced in the bremsstrahlung off nuclei due to the $\gamma - A'$ mixing (see Fig. 1) and subsequently decay invisibly ($A' \rightarrow invisible$):

$$e^- Z \rightarrow e^- Z A', \quad A' \rightarrow invisible \quad (4)$$

The A' -production cross section in this process was calculated [6] in the Weizsäcker-Williams (WW) approximation [21], namely

$$\begin{aligned} \frac{d\sigma}{dx d\cos\theta_{A'}} &= \frac{8Z^2\alpha_{QED}^3\epsilon^2 E_0^2 x}{U^2} \frac{\chi}{Z^2} \\ &\left[(1-x+x^2/2) - \frac{x(1-x)m_{A'}^2 E_0^2 x \theta_{A'}^2}{U^2} \right], \end{aligned} \quad (5)$$

where E_0 is the energy of incoming electron, $E_{A'}$ is the energy of A' , $E_{A'} = xE_0$, $\theta_{A'}$ is the angle in the lab frame between the emitted A' and the incoming electron, Z is the atomic number of nucleus ($Z = 82$ for lead). The function $U = U(m_{A'}, E_0, Z, A)$ which determines the virtuality of intermediate electron has the following form:

$$U = E_0^2 x \theta_{A'}^2 + m_{A'}^2 \frac{1-x}{x} + m_e^2 x. \quad (6)$$

The effective flux of photons, $\zeta = \zeta(m_{A'}, E_0, Z, A)$ is defined as follows:

$$\zeta = \int_{t_{min}}^{t_{max}} dt \frac{t - t_{min}}{t^2} G_2(t), \quad (7)$$

where $t = -q^2$, $|\vec{q}| = U/(2E_0(1-x))$, $t_{min} \simeq |\vec{q}|^2$, $t_{max} = m_{A'}^2$, and $G_2(t) = G_{2,el}(t) + G_{2,in}(t)$ is the sum of elastic and inelastic electric form factor (for details see

e.g. Ref. [6] and references therein). In the numerical integration (7) we neglect x - and $\theta_{A'}$ -dependences of t_{min} .

Several additional remarks should be made. First, the approximation of collinear A' emission is justified for the benchmark points, $m_{A'} \lesssim 1$ GeV and $E_0 \lesssim 100$ GeV, when $m_{A'}/E_0 \ll 1$ (see Ref. [6] for details). Second, one can perform the cross-section (5) integrated over x and $\theta_{A'}$,

$$\sigma_{tot} \simeq \frac{4}{3} \frac{\alpha^3 \epsilon^2 \zeta}{m_{A'}^2} \log(\delta^{-1}), \quad (8)$$

where $\delta = \max(m_{A'}^2/E_0^2, m_e^2/m_{A'}^2)$ is the infrared (IR) cut-off of the cross-section, which regulates either soft intermediate electron singularity or validation of WW approximation [6].

In order to determine the acceptance of the experiment we perform the signal Monte Carlo simulation. We simulate the electromagnetic shower development in the ECAL with **GEANT4** using the following steps

- (i) calculate the total and differential cross-sections of the A' bremsstrahlung production (5) as a function of the electron energy E_0 ,
- (ii) at each step of electron in the lead converters of the ECAL we apply the John von Neuman sampling algorithm of rejecting or accepting the emission of A'
- (iii) if the emission is accepted, we randomly generate values of x and $\cos\theta$ and apply the John von Neuman sampling algorithm of rejecting or accepting x and $\cos\theta_{A'}$,
- (iv) randomly sample the azimuthal angle $\phi_{A'}$,
- (v) calculate 4-momentum of the recoil electron.

We use the signal selection cut $E_{mis}^e = E_0 - E_{detected} > E_0/2$, where E_0 is the electron beam energy, $E_0 = 100$ GeV. E_{mis}^e is approximately equal to $E_{A'}$, small difference is only caused by the finite ECAL energy resolution.

In Fig. 2 an example of the A' energy distributions calculated for masses $m_{A'} = 10$ MeV and $m_{A'} = 500$ MeV are shown. Note that these distributions represent also the missing energy spectra in the detector.

III. THE DETECTOR

The A' production is a rare event. For the interesting parameter range it is expected to occur with a rate $\lesssim 10^{-9}$ with respect to the ordinary photon production

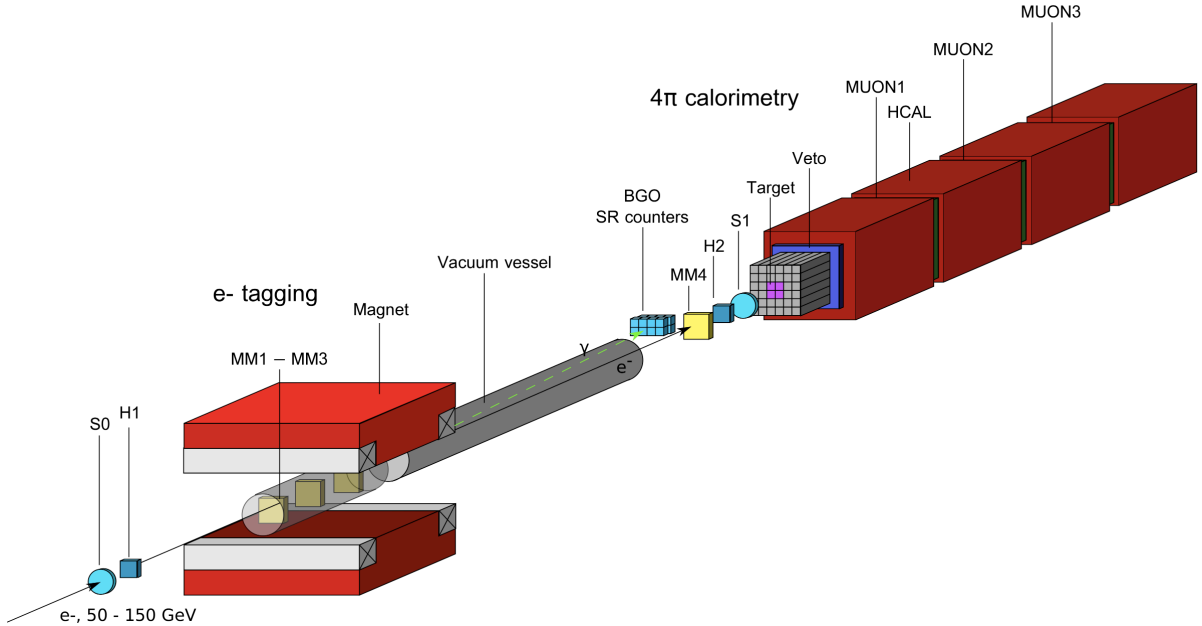


FIG. 3: Schematic illustration of the setup to search for $A' \rightarrow \text{invisible}$ decays with 100 GeV e^- at H4 beam. The incident electron energy absorption in the ECAL is accompanied by the emission of bremsstrahlung A' 's in the reaction $eZ \rightarrow eZA'$ of electrons scattering on nuclei, see Fig. 1. The part of the primary beam energy is deposited in the ECAL, while the remaining fraction of the total energy is transmitted by the decay dark matter particles through the rest of the detector. The A' 's penetrate the ECAL, veto V and HCAL without interactions resulting in the missing energy signature in the detector.

rate. Hence, its observation represents a challenge for the detector design and performance.

The experimental setup specifically designed to search for the A' production in the reaction (4) of high-energy electron scattering off nuclei in a high density target T is schematically shown in Fig. 3. The experiment employs the upgraded H4 electron beam line at the CERN SPS described in details in Ref.[22]. The beam is designed to transport the electrons with the maximum intensity $\simeq 10^6$ in the momentum range between 80 and 100 GeV/c that could be produced by the primary proton beam of 450 GeV/c with the intensity up to a few 10^{12} protons on target per SPS spill. The electrons are produced by protons impinging on a primary beryllium target and transported to the detector inside the evacuated beam-line tuned to an adjustable beam momentum. The hadron contamination in the electron beam is $\pi/e^- \lesssim 10^{-2}$ and the size of the beam at the detector position is of the order of a few cm^2 .

The detector shown in Fig. 3 utilizes upstream magnetic spectrometers (MS) consisting of dipole magnets and a low-material-budget tracker, which is a set of Micromegas chambers, MM1-MM4, allowing the reconstruction and precise measurements of momenta for incident electrons [23]. It also uses the scintillating counters S0, S1 and hodoscopes H1 and H2 to define the primary beam, and the active target T , which is the central part of the high-efficiency hodoscopic elec-

tromagnetic calorimeter (ECAL) used for the accurate measurement of the the recoil electron energy from the reaction (4). Downstream the target the detector is equipped with high-efficiency forward veto counter V, and a massive, completely hermetic hadronic calorimeter (HCAL). Three straw-tubes chambers, MUON1-MUON3, located between the HCAL modules are used for the final-state muon(s) identification. The modules serve as a dump to completely absorb and detect the energy of hadronic secondaries produced in the electron interactions $e^- A \rightarrow \text{anything}$ in the target. In order to suppress backgrounds caused by the detection inefficiency the HCAL must be longitudinally completely hermetic [19, 20]. To enhance its hermeticity, the HCAL thickness is chosen to be $\simeq 30 \lambda_{int}$ (nuclear interaction lengths). The 15 m long vacuum vessel between the magnet and the ECAL is installed to avoid absorption of the synchrotron radiation photons detected at the downstream end of the vessel by the array of BGO crystals for the effective tagging of the incoming beam electrons [19].

IV. MISSING ENERGY SIGNATURE OF SIGNAL EVENTS

The method of the search is the following [19]. The reaction (4) typically occurs in the first few radiation

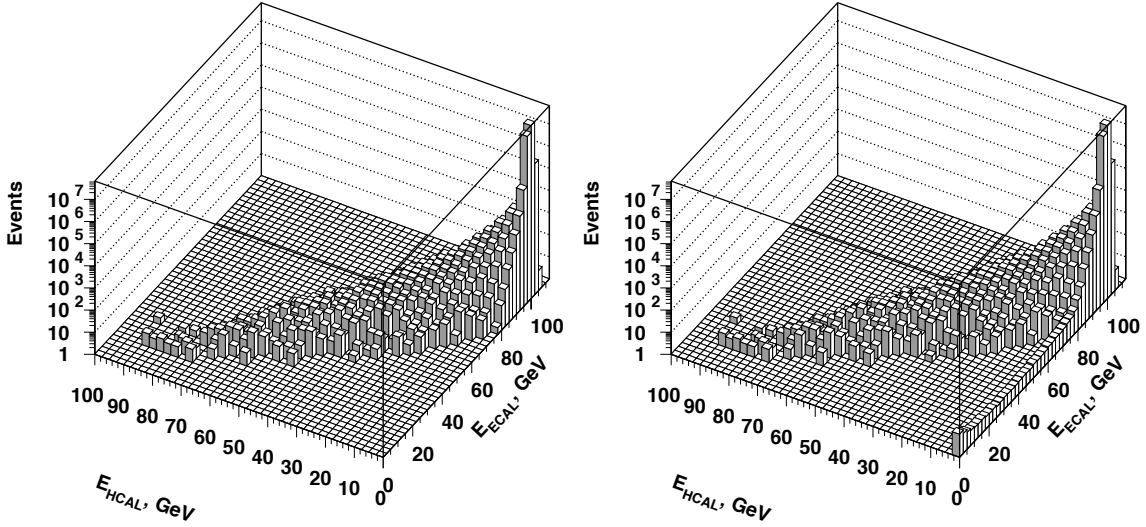


FIG. 4: Expected distributions of events from the reaction (4) in the $(E_{ECAL}; E_{HCAL})$ plane without the signal (left plot) and with the A' emission (right plot). Every event in the left plot satisfies within the uncertainties the constraint $E_{ECAL} + E_{HCAL} = E_0$. In the right plot the events from the region $0 \lesssim E_{ECAL} \lesssim 80$ GeV, $E_{HCAL} \lesssim 1$ GeV have $E_{ECAL} + E_{HCAL} < E_0$ due to the loss of a significant fraction of energy which is carried away by A' s. The A' energy spectrum is calculated for the mixing value $\epsilon \simeq 10^{-2}$ and mass $M_{A'} = 50$ MeV.

length (X_0) of the ECAL. The part of the primary beam energy is deposited in the ECAL, while the remaining fraction is transmitted by the decay particles χ through the rest of the detector. As the χ s are very weakly interacting particles, they penetrate the ECAL, veto V and the HCAL without interactions resulting in the missing energy signature in the detector. The occurrence of $A' \rightarrow \text{invisible}$ decays would appear as an excess of events with a single e-m showers in the ECAL, Fig. 3, and zero energy deposition in the rest of the detector, above those expected from the background sources. The signal candidate events have the signature:

$$S_{A'} = H1 \times H2 \times ECAL(E_{ECAL} < E_0) \times \overline{V \times HCAL}, \quad (9)$$

and should satisfy the following selection criteria:

- (i) The momentum of the incoming particle track should correspond to the beam momentum.
- (ii) The starting point of the (e-m) shower in the ECAL should be localized within a few first X_0 s.
- (iii) The lateral and longitudinal shape of the shower in the ECAL is consistent with the one expected for the signal shower. The fraction of the total energy deposition in the ECAL is $f \lesssim 0.5 - 0.7$, where E_0 is the benchmark electron beam energy, $E_0 = 100$ GeV. This implies the selection condition for the recoil electron $E'_e < 50$ GeV. Therefore, the

missing energy $E_{mis} = E_{A'} = E_0 - E_{ECAL}$ should be $E_{mis}^e = E_{A'} > E_0/2$.

- (iv) No energy deposition in the V and HCAL.

In Fig. 4 the expected distributions of the energy deposition in the $(E_{ECAL}; E_{HCAL})$ plane from the reaction (4) with (rhs plot) and without (lhs plot) A' emission are shown. One can see that the experimental signature of the A' production in the reaction (4) is an event with the missing energy $E_{miss} \gtrsim E_0 - E_{ECAL}^{th}$ from the region $0 \lesssim E_{ECAL} \lesssim E_{ECAL}^{th}$ and $0 \lesssim E_{HCAL} \lesssim E_{HCAL}^{th}$. The typical values for the ECAL and HCAL threshold energies are expected to be $E_{ECAL}^{th} \simeq 50$ GeV, i.e. $E_{miss} > 50$ GeV, and $E_{HCAL}^{th} \simeq 0.3$ GeV, respectively. The events in this region are supposed to be from the reaction (4) as a large fraction of the primary beam energy is carried away by the A' , those spectrum shown in Fig. 4 for $M_{A'} = 50$ MeV, and mixing strength $\epsilon \simeq 10^{-2}$. For the ECAL, the value of E_{ECAL}^{th} is defined by the shape of the low energy tail of the ECAL response function to the monochromatic electron beam. This tail is mostly due to i) the longitudinal fluctuations of the e-m shower development and corresponding leak energy, and ii) electroproduction of hadrons by primary electrons in the target. The E_{HCAL}^{th} value is defined mostly by the noise level of the HCAL electronics, energy leak from the ECAL, and pileup events, see Section V.

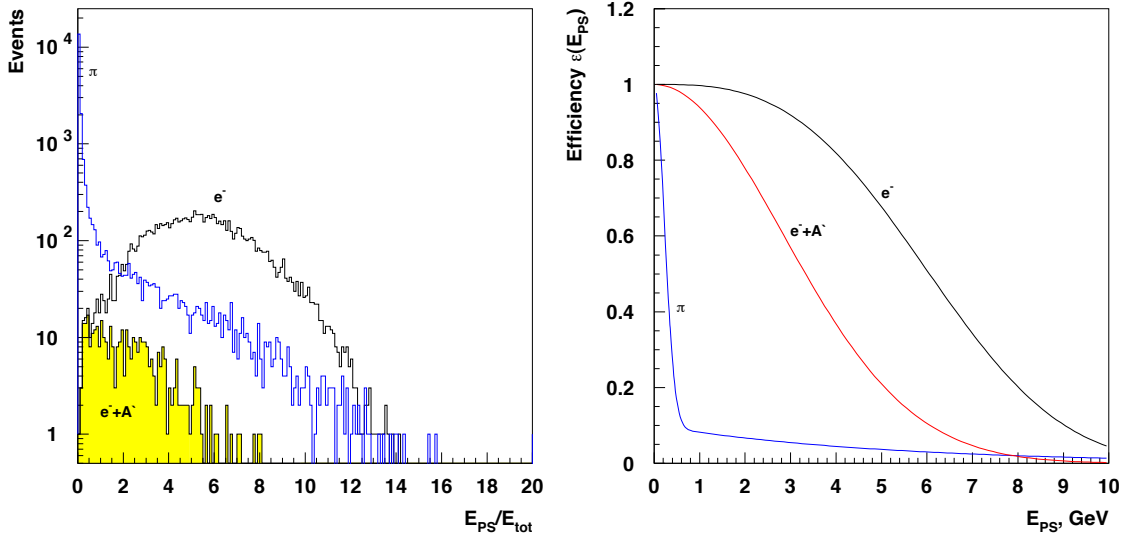


FIG. 5: Expected distributions of the energy deposited in the ECAL preshower from 100 GeV pions (blue), electrons (black) and signal events (shaded) (lhs plot). The energy spectrum of A' 's emitted in the reaction (4) is calculated for the mixing strength $\epsilon \lesssim 1$, mass $M_{A'} = 50$ MeV, and $E_{miss} \gtrsim 0.5E_0$. The rhs plot shows the pion, electron and signal efficiency as a function of threshold on the E_{PS} value.

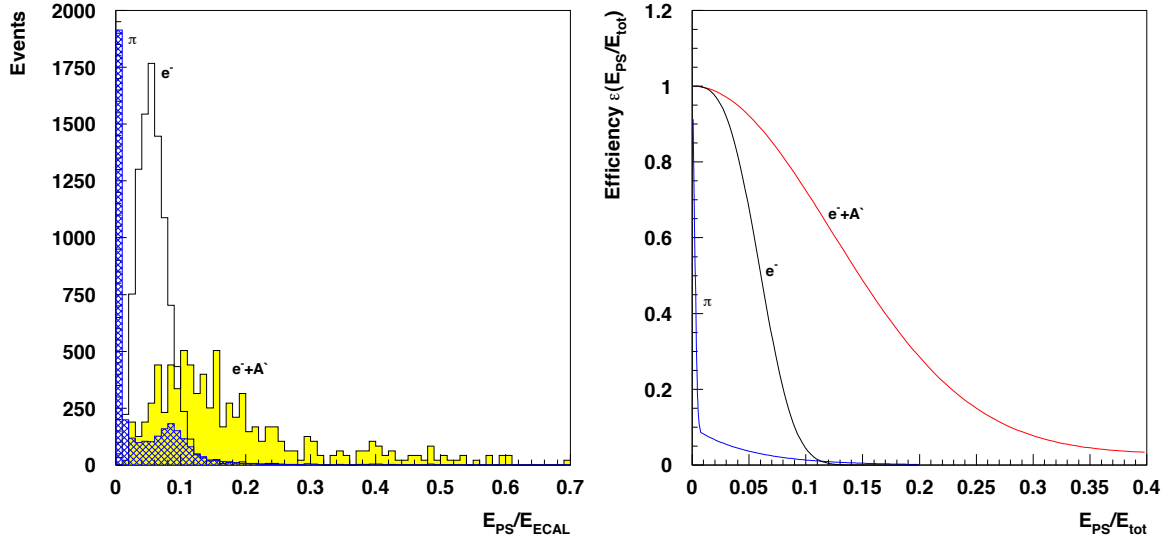


FIG. 6: Expected distributions of the E_{PS}/E_{ECAL} ratio of energy deposited in the ECAL preshower to the total energy deposited in the ECAL (lhs plot) from 100 GeV pions (blue), electrons (black) and signal events (shaded). The energy spectrum of A' 's emitted in the reaction (4) is calculated for the mixing strength $\epsilon \lesssim 1$, mass $M_{A'} = 50$ MeV, and $E_{miss} \gtrsim 0.5E_0$. The rhs plot shows the pion, electron and signal efficiency as a function of threshold on the E_{PS}/E_{ECAL} value

V. THE ECAL RESPONSE TO THE SIGNAL EVENTS

The use of the ECAL is twofold. On the one hand, it serves as an active target to measure the total energy deposition in the beam dump. On the other hand, it

has longitudinal and lateral granularity allowing additional suppression of the hadronic background by studying the shower shape. Simulations show that by using the electromagnetic and hadronic shower profiles in the calorimeters, both lateral and longitudinal, it is possible to further improve the e/π rejection by a factor of 5-10.

Longitudinally the ECAL is subdivided in two parts: preshower and absorption part. The preshower has 4 radiation lengths of lead and plays an important role in the hadron background rejection obtainable with the ECAL. Hadron rejection is ultimately limited by such processes as charge exchange ($\pi^\pm + N \rightarrow n\pi^0 + N'$) where most of the energy of the charged pion goes to one or more neutral pions. The π^0 s immediately decays into photons starting a cascade shower which is indistinguishable from the electron-initiated shower. Thus, charge exchange interactions of the beam pions occurring near the front of the ECAL array and accompanied by a poor detection of the rest of the final state cannot be separated from the reaction (4) [19]. The additional suppression of such processes can be provided by using the lead as the calorimeter passive material (it has a smaller number of interaction lengths per radiation length) by the requirement of the early development of the shower. The A' events are supposed to be reconstructed in the ECAL as electromagnetic showers. Therefore, the question arises to what extent the properties of the electromagnetic shower in the ECAL from the reaction (4) are identical to the properties of the ordinary shower induced by an electron with the same energy deposition in the ECAL. For example, one could suggest that the emission of a high-energy A' could make the residual electromagnetic shower development slightly asymmetric resulting in modification of the lateral shower profile exceeding the ordinary shower fluctuations. This could change the selection efficiency of the cuts iii) of Section IV. To answer this question we have compared the lateral and longitudinal electromagnetic shower profiles in the ECAL for ordinary and signal electromagnetic showers induced by the reaction (4). In this study the shashlik ECAL used in simulations has the following characteristics:

- (i) It is a matrix of 6x6 cells, each with dimensions $38.2 \times 38.2 \times 490 \text{ mm}^3$.
- (ii) Each cell is (1.50 mm Pb + 1.50 mm Sc) x 150 layers or 40 radiation length (X_0).
- (iii) Each cell is longitudinally subdivided into two parts: preshower section (PS) of 4 X_0 and the main ECAL of 36 X_0 .
- (iv) The simulated energy resolution is $\sigma E/E \simeq 9\%/\sqrt{E(\text{GeV})} + 0.7$

A. Longitudinal shower development

One of the sources of background is expected from hadron interactions in the ECAL that could mimic the signal [19]. The electron-hadron separation in this

case can be improved if we measure the electromagnetic shower development at an early stage by using the ECAL preshower section. Then the question arises how identical are the longitudinal development of showers induced by the signal reaction (4) and by an ordinary electron and how the applied hadron rejection cuts affect the signal efficiency. In this section, we take a step toward answering this question. We examine the qualitative features associated with the longitudinal distributions of deposited energy by showers induced by pions, electrons and signal events, and assess to what extent these features are affected by dark-photon emission for the signal events.

We use variable $r = E_{PS}/E_{tot}$ - the ratio of the energy deposit in the PS to the total energy deposit E_{tot} - to evaluate the pion rejection factors at given electron and signal efficiencies. The distribution of energy E_{PS} deposited in PS and the r ratios for 100 GeV showers induced by the pions, electrons, and signal events is shown in the lhs of Fig. 5 and Fig. 6, respectively. The electron, pion and signal efficiencies as functions of the threshold on the E_{PS} and r values are shown in the rhs of Fig. 5 and Fig. 6, respectively. For the signal events the calculations are performed for $E_{miss} > 0.5E_0$. One can see that for the A' case the fluctuations of the E_{PS}/E_{tot} ratio are significantly large then for the electron case: the r value ranges from 0 to 0.6, while for the electron induced events it is in the region $0 < r < 0.1$. Interestingly, for the same threshold E_{PS}^{th} on the E_{PS} value, the electron efficiency $\epsilon_e(E_{PS}^{th})$ is higher than the signal one, $\epsilon_{A'}(E_{PS}^{th})$ as shown in Fig. 6. In order to keep $\epsilon_{A'}(E_{PS}^{th}) \gtrsim 0.9$ the threshold should be $E_{PS}^{th} \lesssim 1 \text{ GeV}$. However, for the same threshold r^{th} , the situation is opposite, and the signal efficiency is higher compared to the electron one, $\epsilon_{A'}(r^{th}) > \epsilon_e(r^{th})$, as shown in Fig. 6. This is because the emission of the A' with the energy $E_{A'} > 0.5E_0$ is typically occurs in the early stages of the electromagnetic shower development. After the A' emission, the residual shower has much lower energy than the primary electron energy, and thus is also shorter in length. Therefore, larger fraction of its energy is deposited in the first PS part of the ECAL.

B. Lateral shower development

Fig. 7 shows the simulated dependence of the average ratio E_i/E_{i+1} of energies deposited in two adjacent counters on the electron coordinate X_e for both electron and signal showers. The coordinate $X = 19.1 \text{ mm}$ corresponds to the centre of the $(i+1)$ th cell of the ECAL, while $X_e = 0$ is the boundary between the i th and $(i+1)$ th cells. With the obtained dependence of the ratio E_i/E_{i+1} on X_e one can define the shower profile $E(X_e)$,

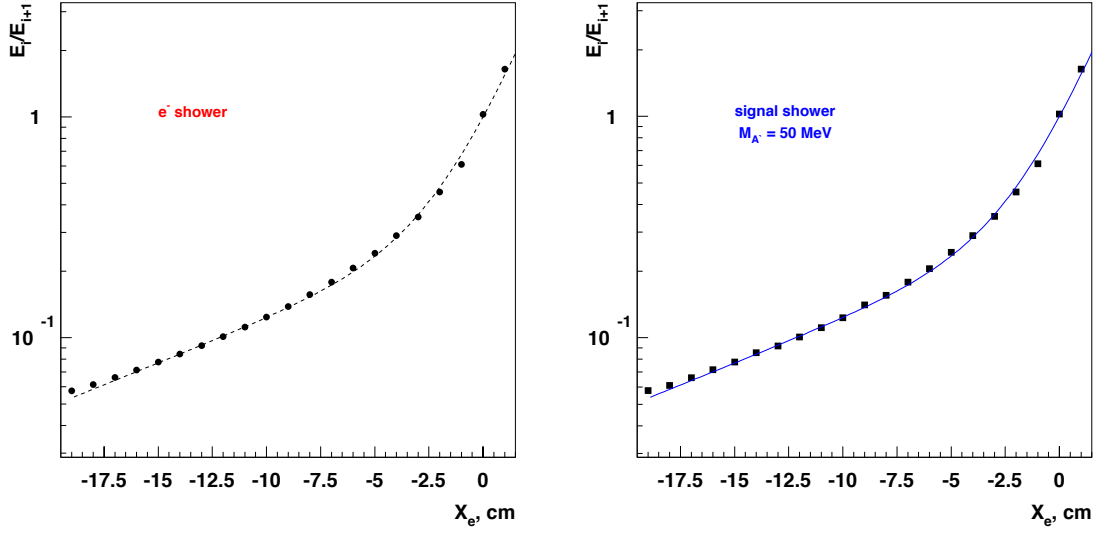


FIG. 7: Expected dependence of the ratio E_i/E_{i+1} of the average energies deposited in two adjacent cells on electron coordinate X_e for the electromagnetic showers induced by the beam electrons without (left plot) and with (right plot) the A' emission from the reaction (4). Shown are the simulated values, the curves have been calculated for the lateral shower profile of Eq.(7), with $b_1 = 2.5 \pm 0.3$ mm, $b_2 = 12 \pm 2$ mm, and $a_2/a_1 = 0.42 \pm 0.12$ for the ordinary shower and $b_1 = 2.4 \pm 0.3$ mm, $b_2 = 11 \pm 2$ mm, and $a_2/a_1 = 0.45 \pm 0.12$ for the signal shower.

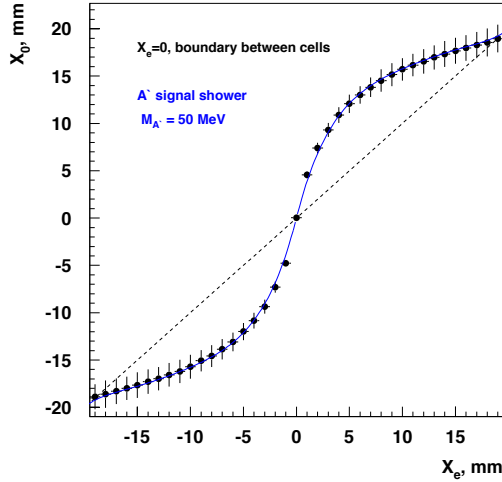


FIG. 8: The calculated with Eq.(11) coordinates of the shower centre-of-gravity X_0 at different positions of the true coordinate X_e of incoming electrons. The position $X_e = 0$ corresponds to the cell centre. Dots show the reconstructed values for X_0 , the error bars represents uncertainties (σ_X) in the coordinate X_c reconstruction. The curve has been calculated with Eq.(10).

which is the energy release as a function of the distance from the shower axis well described by two exponential

functions:

$$E(x_e) = a_1 \exp(-|x_e|/b_1) + a_2 \exp(-|x_e|/b_2) \quad (10)$$

The fit shown in Fig. 7 results in $b_1 = 2.1 \pm 0.3$ mm, $b_2 = 12.3 \pm 1.3$ mm and $a_1/a_2 = 0.14 \pm 0.03$ for electron and $b_1 = 2.1 \pm 0.3$ mm, $b_2 = 12.3 \pm 1.3$ mm and $a_1/a_2 = 0.14 \pm 0.03$ for signal events, which are in good agreement with each other.

The simplest method to determine the coordinates of high energy photons and electrons in a granular calorimeter is to measure the "center of gravity" X_0 of the electromagnetic shower induced by them:

$$X_0 = 2\Delta \sum_i i E_i / \sum_i E_i, \quad (11)$$

where Δ is the half-width of the ECAL cell. In Fig. 8 the calculated with Eqs.(10,11) coordinates of the shower centre-of-gravity X_0 at different positions of the true coordinate X_e of incoming electrons are shown. The position $X_e = 0$ for this case corresponds to the cell centre. Dots show the reconstructed values for X_0 , the error bars represent uncertainties (σ_X) in the coordinate X_c reconstruction. The reconstructed X -coordinate of the signal e-m showers for both cases shown in Fig. 9 are shifted with respect to the true coordinate of the primary electron X_e . The distributions are found to be very similar to each other. For example, they are practically identical for the beam positioned at the boundary

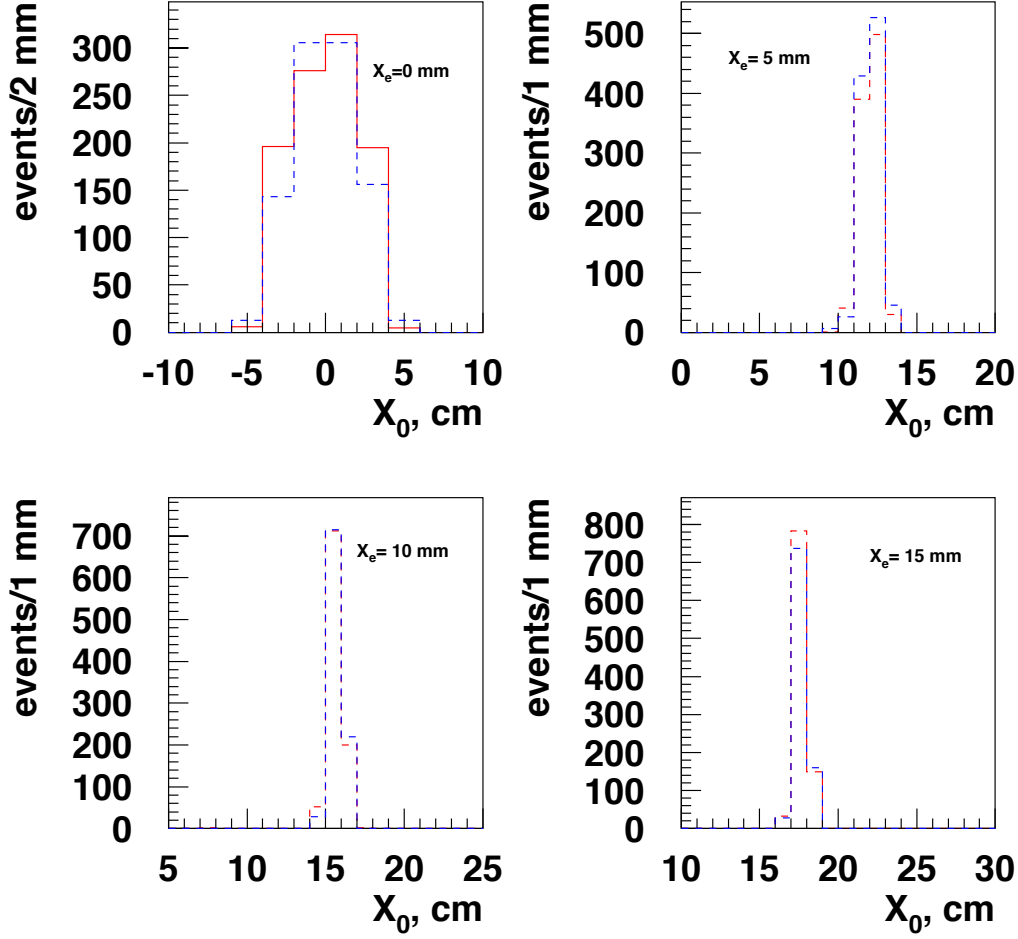


FIG. 9: The calculated with Eqs.(10, 11) coordinates of the shower centre-of-gravity X_0 at different positions of the true coordinate X_e of incoming electrons. The position $X_e = 0$ corresponds to the cell centre. Dots show the reconstructed values for X_0 , the error bars represents uncertainties (σ_X) in the coordinate X_e reconstruction. The curve has been calculated with Eq.(10).

between the cells, where the difference due to transverse shower fluctuations is expected to be most significant. The deviation from linearity is due to the two-exponential shape of the e-m shower profile in the ECAL calculated with Eq.(10) for pure electron and signal events. One can see that both dependences are very similar. This nonlinearity can be corrected with technique described e.g. in Ref.[27, 28]. From Fig. 9 we conclude that the shape selection efficiency for signal events with given X,Y cuts will not differ from the efficiency for pure electrons with the same energy deposition in ECAL.

As discussed previously, simulations of the energy response to hadrons show that there is a non-zero probability that the observed energy deposition, e.g. of a

pion is consistent with that of an electron. The lateral shower shape information can also be used to reduce the probability of primary electron misidentification. The energy weighted average radius for the shower in the ECAL can be defined as:

$$r = \frac{\sum_i E_i [(x_i - \langle x \rangle)^2 + (y_i - \langle y \rangle)^2]^{1/2}}{\sum_i E_i}, \quad (12)$$

The simulations of the r -value for both cases also agree well.

Finally, the main conclusion of this study is that while the properties of electromagnetic showers induced by the signal and ordinary electrons are practically identical for the lateral shower development, the use of selection cuts on longitudinal shower development in the

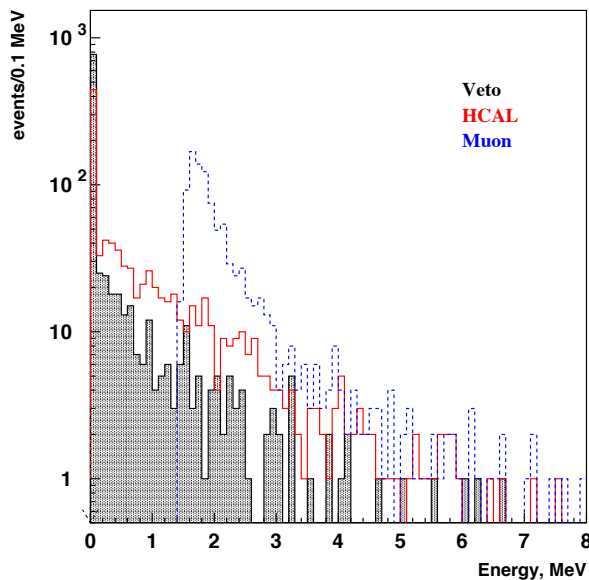


FIG. 10: The calculated distribution of energy deposited in the Veto and HCAL from the reaction (4). The distribution of the energy released in the Veto by a muon is also shown for comparison.

ECAL results in significant corrections for the signal efficiency.

TABLE I: Expected signal efficiencies vs selection cuts calculated for the $A' \rightarrow \text{invisible}$ decay of A' with the mass $M_{A'} = 100$ MeV (see text for details).

Selection cut	Expected efficiency
Preshower $E_{PS}/E_0 \gtrsim 0.03$	$\gtrsim 0.95$
$E_{miss}/E_0 \gtrsim 0.5$	$\gtrsim 0.93$
ECAL X,Y matching	$\gtrsim 0.90$
e/π rejection, ECAL shower shape	$\gtrsim 0.90$
VETO energy $E_V \lesssim 1$ MeV	$\gtrsim 0.95$
HCAL energy $E_{HCAL} \lesssim 0.1$ GeV	$\gtrsim 0.95$
Total efficiency, ϵ_{eff}	$\gtrsim 0.65$

C. The Veto and HCAL response to signal events

One of the main variables defining the sensitivity of the experiment is the effective width of the signal event distribution, shown in Fig. 4, along the E_{HCAL} -axis. The spread of the energy deposition of signal events in the HCAL is defined by the energy leak from the shower tail due to fluctuations the longitudinal shower development and also by the admixture of the pile-up events.

The hadronic calorimeter is a set of four modules. Each module is a matrix of 3×3 cells. Each cell is a sandwich of alternating layers of steel and scintillator plates with thicknesses of 25 mm and 4 mm, respectively, and with a lateral size of 194×192 mm². Each cell consists of 48 such layers and has a total thickness of $\simeq 7\lambda_{int}$. The amount of the leak energy from the ECAL to the HCAL depends on the primary beam energy. The thickness of the ECAL was chosen using the full shower simulation to minimize the amount of energy that leak into the Veto and HCAL. The purpose was to reduce it down to the level below a few tens of MeV (the PED width of the HCAL electronics). In Fig. 10 the spectrum of the leak energy is shown.

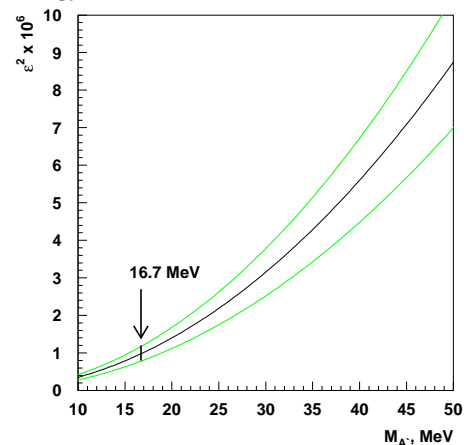


FIG. 11: The dependence of the mixing ϵ^2 as a function of $M_{A'}$ obtained for the $n_{A'} \simeq 1.1 \cdot 10^2$ observed events accumulated with $\simeq 2 \cdot 10^{10}$ eot. The green curves represent the 90% C.L.. Assuming that the observed events originated from decays of A' with mass $M_{A'} = 16.7$ MeV would result in determination of mixing strength interval around $\epsilon \simeq 10^{-3}$ value indicated by the arrow.

VI. EXPECTED RESULTS

In this section we consider two possible outcomes of the experiment: A) observation of an excess of signal events associated with the reaction (4), B) no excess of signal events is observed.

A. Extraction of the parameters $M_{A'}$ and ϵ using the missing energy spectrum.

For the case of signal observation we performed a pseudo-experiment aiming at the study of the possibility of extraction of the parameters $M_{A'}$ and ϵ . As an example, we consider benchmark values for the A' mass $M_{A'} = 16.7$ MeV and mixing strength $\epsilon \simeq 10^{-3}$, which

$m_{A'}, \text{MeV}$	(A)		(B)		(C)	
	$N_{eot} = 10^9$	$N_{eot} = 10^{12}$	$N_{eot} = 10^9$	$N_{eot} = 10^{12}$	$N_{eot} = 10^9$	$N_{eot} = 10^{12}$
2	$1.33 \cdot 10^{-4}$	$4.20 \cdot 10^{-6}$	$3.40 \cdot 10^{-4}$	$1.07 \cdot 10^{-5}$	$3.61 \cdot 10^{-4}$	$1.20 \cdot 10^{-5}$
10	$3.91 \cdot 10^{-4}$	$1.23 \cdot 10^{-5}$	$8.14 \cdot 10^{-4}$	$2.57 \cdot 10^{-5}$	$8.98 \cdot 10^{-4}$	$2.73 \cdot 10^{-5}$
50	$1.44 \cdot 10^{-3}$	$4.57 \cdot 10^{-5}$	$3.48 \cdot 10^{-3}$	$1.10 \cdot 10^{-4}$	$4.26 \cdot 10^{-3}$	$1.29 \cdot 10^{-4}$
500	$1.84 \cdot 10^{-2}$	$5.83 \cdot 10^{-4}$	$5.12 \cdot 10^{-2}$	$1.61 \cdot 10^{-3}$	—	$2.77 \cdot 10^{-3}$

TABLE II: Upper bounds on mixing ϵ at 90 % CL for the following cases: (A): this work, Pb-Sc dump, $E_{miss} > 0.5E_0$, $E_0 = 100$ GeV; (B): this work, W-Sc dump, $E_{miss} > 0.9E_0$, $E_0 = 10$ GeV; (C): IKST, W-dump, $E_{miss} > 0.9E_0$, $E_0 = 10$ GeV.

are motivated by the results of the recent experiment Ref.[15]. Two possibilities were considered.

For the case of a signal observation with a limited statistics of 10 - 100 events it would be possible to determine a band of allowed ϵ values in the two-dimensional plot (ϵ , $M_{A'}$). This could be done as follows. The observed number of signal events $n_{A'}$ passing the selection cuts is distributed according to Poisson statistics

$$P(n_{A'}, \lambda) = \frac{\lambda^{n_{A'}}}{n_{A'}!} e^{-\lambda} \quad (13)$$

where $\lambda = \langle n_{A'} \rangle$ is the average number of signal events. The λ depends in particular on ϵ , $M_{A'}$, E_e , n_{eot} - the total number of electrons on target, and other parameters related to the target. It can be expressed in the form

$$\lambda = \frac{n_{eot} \lambda_0}{10^{12}} \left(\frac{\epsilon}{10^{-5}} \right)^2 \left(\frac{10 \text{ MeV}}{M_{A'}} \right)^2 \quad (14)$$

where parameter λ_0 depends rather weakly (logarithmically) on $M_{A'}$ and E_0 and is $\lambda_0 = 1.52$ for $M_{A'} \simeq 10$ MeV and $E_0 = 100$ GeV.

If $\lambda \gg 1$ the Poisson distribution is approximated by the Normal distribution. Hence, for given (ϵ , $M_{A'}$), the number of signal events at "one-sigma" confidence level is given by

$$\lambda - \sqrt{\lambda} \leq n_{A'} \leq \lambda + \sqrt{\lambda} \quad (15)$$

Using inequality (15) and the expression for the parameter λ given by

$$\lambda \simeq \frac{\epsilon^2}{M_{A'}^2} \lambda_1(M_{A'}), \quad (16)$$

we can estimate from the data the ratio $\frac{\epsilon^2}{M_{A'}^2}$. An example of such estimate for $\epsilon \simeq 10^{-3}$, $M_{A'} = 16.7$ MeV, and $n_{eot} \simeq 2 \cdot 10^{10}$ is shown in Fig. 11. In this case one can expect to observe $n_{A'} \simeq 1.1 \cdot 10^2 \pm 11$ signal events. Using the dependence of the mixing ϵ^2 on the mass $M_{A'}$ shown, one can cross-check the results of Ref.[15] by estimating the value of ϵ for the benchmark A' mass value.

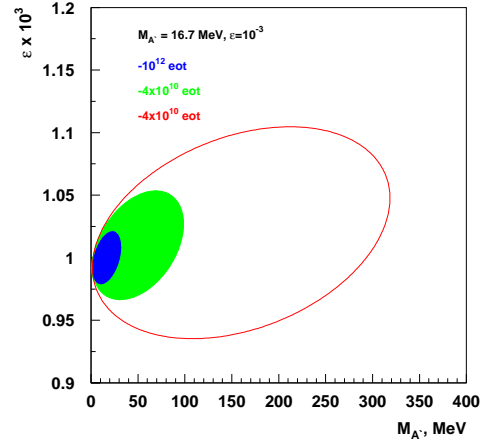


FIG. 12: The fitted $\Delta\chi^2 = 1$ contours in the ϵ vs $m_{A'}$ plane for invisibly decaying A' obtained from the fit of E_{miss} spectra calculated for the A' masses, $M_{A'} = 16.7$ MeV and mixing $\epsilon = 10^{-3}$ and the missing energy $E_{miss} > 0.2E_0$ for $4 \cdot 10^{10}$ (green area) and 10^{12} (blue area) eot, respectively. The red contour is calculated for the $E_{miss} > 0.5E_0$ and $4 \cdot 10^{10}$ eot.

In case of a signal observation with a higher statistics $n_{A'} \gtrsim 10^3$ events ($n_{eot} \simeq 10^{12}$) it should be possible to perform more precise measurement of the correlated parameters ϵ and $M_{A'}$. This measurement is based on Eq.(8) and the dependence of the shape of the missing energy spectrum on $M_{A'}$, as shown in Fig. 2. The later is rather weak, and is significant only in a missing energy range around $E_{miss} \simeq 0.2$. In this study, we assume that the E_{miss} shape in this region is determined only by statistical errors, however poorly predictable background can be also present. Two intervals of missing energy $0.5E_0 < E_{miss} < E_0$ and $0.2E_0 < E_{miss} < 0.5E_0$ were considered for comparison.

Then, the following steps are made. On a grid of different ϵ and $M_{A'}$ parameters for each point we performed comparison of the E_{miss} distribution from "observed" number of events with the simulated spectra. The Kolmogorov and χ^2 tests, used for the shape compatibility check, give rather similar results. The al-

lowed regions with probabilities (p-values) expressed in terms of the corresponding numbers of standard deviations were finally obtained. In Figure 12 an example of the one standard deviation "ellipse" contour for the best fit parameters for the different thresholds on E_{miss} and numbers of accumulated eot is shown. The best fit parameters are found to be $M_{A'} = 16.3$ MeV and $\epsilon = 0.985 \times 10^{-3}$ for the $n_e \simeq 10^{12}$. The estimated sensitivity of the search allows either to observe the $16.7 A'$ or exclude the dark photon interpretation of the excess events within a few months of running.

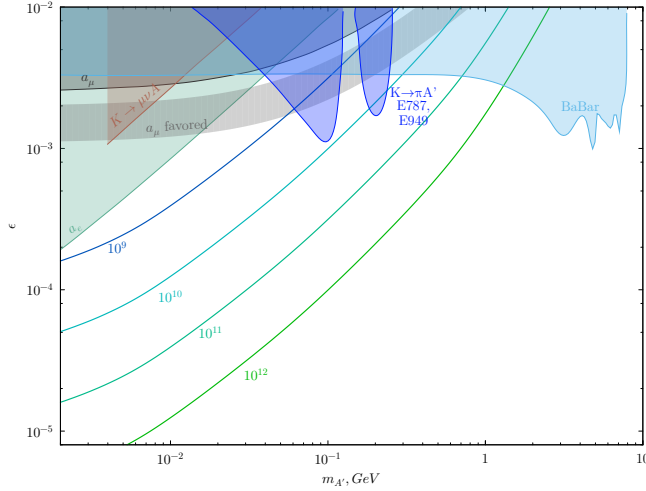


FIG. 13: Exclusion region in the $(M_{A'}, \epsilon)$ plane expected from the results of the proposed experiment for 10^9 , 10^{10} , 10^{11} and 10^{12} incident electrons at the energy $E_0 = 100$ GeV. Direct constraints from the BaBar [11, 24], and E787+E949 experiments [13, 25], as well as muon (g-2) favored area are also shown. The figures are based on Ref.[26]. For more limits obtained from indirect searches and planned measurements see e.g. Ref. [7].

B. Expected sensitivity

In this section we consider expected bounds on dark photon parameter space based on the **GEANT4** MC simulation of the A' yields in the NA64 experiment. We define the acceptance of the detector η_{acc} as the ratio of signal events with the missing energy $E_{miss} > 0.5E_0$ to the total number of events with a dark photon emitted in the target. The number of signal events from the target is given by

$$n_{A'} = n_{eot} \cdot \frac{\rho N_A}{A_{Pb}} \cdot \epsilon_{eff}(M_{A'}) \cdot \int_{E_0/2}^{E_0} \frac{dn}{dE_{A'}} dE_{A'} \quad (17)$$

where ρ is density of Pb target, N_A is the Avogadro's number, A_{Pb} is the Pb atomic mass, and ϵ_{eff} is the

overall signal selection efficiency, see Table 1. The integration in Eq. (17) is performed over the missing energy spectrum in the ECAL target, see Fig.2.

Using the relation $n_{A'}^{90\%} > n_{A'}$, where $n_{A'}^{90\%}$ is the 90% *CL* upper limit for the number of signal events without background, $n_{A'}^{90\%} = 2.3$, one can determine the expected 90% *CL* bounds on $(M_{A'}, \epsilon)$ parameter space, which are shown in Fig. 13. The bounds are obtained for the total number of electrons on target $n_{eot} = 10^9, 10^{10}, 10^{11}$, and 10^{12} and the electron beam energy $E_0 = 100$ GeV. We assume that the A' 's decays dominantly to the invisible final state.

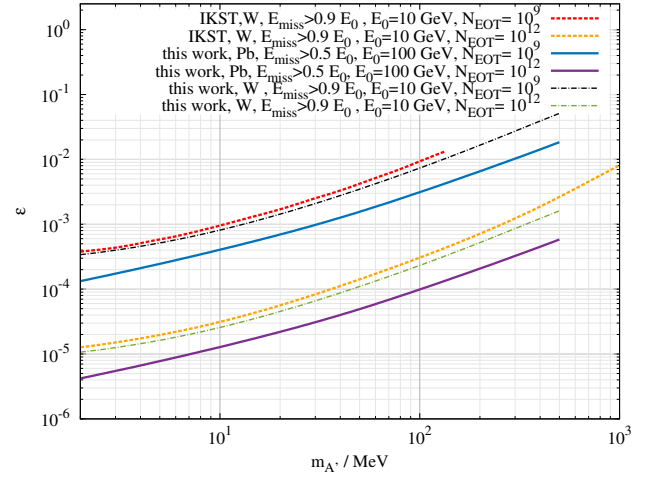


FIG. 14: Comparison of the upper limits in the ϵ vs $m_{A'}$ plane for invisibly decaying A' calculated for the W-ECAL target [20], $E_0 = 10$ GeV, and the missing energy $E_{miss} > 0.9E_0$ by Izaguirre et al. [11] (IKST) and in this work for 10^9 eot (red dashed and black dash-dotted), and 10^{12} eot (orange dashed and green dash-dotted), respectively. For comparison limits calculated for the shashlik ECAL target, $E_0 = 100$ GeV, and the ECAL missing energy $E_{miss} > 0.5E_0$ for 10^9 eot (blue solid) and 10^{12} eot (purple solid), respectively, are also shown.

In Fig. 14 and Table II we show detailed comparison of the expected sensitivity for the A' invisible decay search in our experiment calculated in this work with the one evaluated by Izaguirre et al. in Ref.[11] for the case of the W-Sc ECAL and 10^9 eot. The comparison is made for the case of the same type of the ECAL (the W-Sc sandwich calorimeter [19, 20]), the beam energy $E_0 = 10$ GeV, the missing energy range $E_{miss} > 0.9E_0$ and for 10^9 and 10^{12} eot. Our results for the case of the Pb-Sc (shashlik) ECAL, the beam energy $E_0 = 100$ GeV, the missing energy $E_{miss} > 0.5E_0$ and $n_{eot} = 10^9, 10^{12}$ eot are also shown for comparison. For the former case, the expected bounds for tungsten ECAL are in agreement with IKST limits within 10 %. In

Tab. II we show the expected limits on mixing ϵ at 90 % CL for the relevant benchmark masses $m_{A'}$ and ECAL energy thresholds. For the second case, one can see that the sensitivity is two times better than for the former one. This is mainly due to the extension of the allowed missing energy region from $0.5E_0 < E_{miss} < E_0$ to $0.9E_0 < E_{miss} < E_0$ for signal events.

VII. SUMMARY

In this Section, we briefly outline the main improvements achieved in this article with respect to our previous work, as well as the recent work carried out by another group. We have studied the missing energy signature of the production of sub-GeV dark photons in the process of high-energy electron scattering off nuclei in the experiment NA64 aiming at the search for $A' \rightarrow invisible$ decays at the CERN SPS. We have shown the distinctive distributions of these events that serve to distinguish the $A' \rightarrow invisible$ signal from background. The results of the detailed simulations of the detector response and efficiencies to the signal events are presented. The comparison of the lateral shower profiles for the electron and signal events in the ECAL show that they are identical with high accuracy. No significant difference is found. While the longitudinal development of the electron and signal induced showers in the ECAL is quite different. Thus a special attention is required to the selection of a threshold for the energy deposited in the preshower to keep the signal efficiency as high as possible.

Using these results we evaluate the sensitivity of the experiment and show that it allows to probe the still unexplored area of the mixing strength $10^{-6} \lesssim \epsilon \lesssim 10^{-2}$ and masses $M_{A'} \lesssim 1$ GeV. The results obtained are found to be in agreement with the results of Ref.[11]

obtained for the same experimental setup and selection criteria. For a realistic study of the expected sensitivity of the experiment we have improved on two points: we employed the A' production into the GEANT4 simulation package, and performed the full simulation of the detector response to the $A' \rightarrow invisible$ signal events. We re-checked the results of Ref.[11] where the A' yield was carefully derived, and improved it further by taking into account the simulation of the realistic detector configuration, the detector response and the corresponding efficiencies. We believe that the error of the estimates of the experiment sensitivity obtained in those two works is unlikely exceed 10%, which could be attributed to the uncertainty of the A' yield. Taking as a benchmark the $M_{A'} = 16.7$ MeV and $\epsilon = 10^{-3}$ values from the recently found hint at the existence of the $A' \rightarrow invisible$ decay in the nuclear transitions of $^8\text{Be}^*$, we have determined these parameters by fitting Monte Carlo simulated E_{miss} distributions. The best fit parameters are found to be $M_{A'} = 16.3$ MeV and $\epsilon = .985 \times 10^{-3}$ for the $n_e \simeq 2 \cdot 10^{12}$ accumulated eot. We also determined the $\Delta\chi^2 = 1$ contours in the $(M_{A'}, \epsilon)$ parameter space. We demonstrated that estimated sensitivity of the search allows either to observe the 16.7 A' or exclude the dark photon interpretation of the excess events from Ref.[15] within a month of running.

Acknowledgments

We would like to thank members of the NA64 Collaboration for the numerous discussions, and, in particular R. Dusaev and B. Vasilishin for their help. We are grateful to the authors of Ref.[11] for letting us now their results prior the publication, and in particular to P. Schuster for useful comments. The work of D.K. on simulations of signal events has been supported by the RSCF grant 14-12-01430.

-
- [1] L. B. Okun, "Limits Of Electrodynamics: Paraphotons?," Sov. Phys. JETP **56** (1982) 502 [Zh. Eksp. Teor. Fiz. **83** (1982) 892].
 - [2] P. Galison and A. Manohar, "Two Z 's or not two Z 's?", Phys. Lett. B **136** (1984) 279.
 - [3] B. Holdom, "Two $U(1)$'s and Epsilon Charge Shifts," Phys. Lett. B **166**, 196 (1986).
 - [4] N. Arkani-Hamed, D. P. Finkbeiner, T. R. Slatyer and N. Weiner, "A Theory of Dark Matter," Phys. Rev. D **79** (2009) 015014.
 - [5] G. W. Bennett *et al.* [Muon g-2 Collaboration], "Final Report of the Muon E821 Anomalous Magnetic Moment Measurement at BNL," Phys. Rev. D **73** (2006) 072003.
 - [6] J. D. Bjorken, R. Essig, P. Schuster and N. Toro, "New Fixed-Target Experiments to Search for Dark Gauge Forces," Phys. Rev. D **80**, 075018 (2009)
 - [7] R. Essig *et al.*, "Working Group Report: New Light Weakly Coupled Particles", arXiv:1311.0029 [hep-ph].
 - [8] S.N.Gninenko and N.V.Krasnikov, Phys. Lett. B **513**, 119 (2001).
 - [9] P.Fayet, Phys. Rev. D **75**, 115017 (2007).
 - [10] M. Pospelov, "Secluded $U(1)$ below the weak scale," Phys. Rev. D **80** (2009) 095002
 - [11] E. Izaguirre, G. Krnjaic, P. Schuster and N. Toro, "Testing GeV-Scale Dark Matter with Fixed-Target Missing Momentum Experiments," Phys. Rev. D **91**, no. 9, 094026 (2015).
 - [12] M. D. Diamond and P. Schuster, "Searching for Light Dark Matter with the SLAC Millicharge Experiment,"

- Phys. Rev. Lett. **111** (2013) 22, 221803.
- [13] H. Davoudiasl, H. S. Lee and W. J. Marciano, “Muon ($g-2$), rare kaon decays, and parity violation from dark bosons,” Phys. Rev. D **89** (2014) 9, 095006.
 - [14] B. Batell, R. Essig and Z. Surujon, “Strong Constraints on Sub-GeV Dark Sectors from SLAC Beam Dump E137,” Phys. Rev. Lett. **113** (2014) 17, 171802.
 - [15] A. J. Krasznahorkay *et al.*, “Observation of Anomalous Internal Pair Creation in Be8 : A Possible Indication of a Light, Neutral Boson,” Phys. Rev. Lett. **116** (2016) 4, 042501.
 - [16] B. Batell, M. Pospelov and A. Ritz, “Exploring Portals to a Hidden Sector Through Fixed Targets,” Phys. Rev. D **80** (2009) 095024.
 - [17] P. deNiverville, M. Pospelov and A. Ritz, “Observing a light dark matter beam with neutrino experiments,” Phys. Rev. D **84** (2011) 075020
 - [18] R. Dharmapalan *et al.* [MiniBooNE Collaboration], “Low Mass WIMP Searches with a Neutrino Experiment: A Proposal for Further MiniBooNE Running,” arXiv:1211.2258 [hep-ex].
 - [19] S. N. Gninenko, “Search for MeV dark photons in a light-shining-through-walls experiment at CERN,” Phys. Rev. D **89** (2014) 7, 075008
 - [20] S. Andreas *et al.*, “Proposal for an Experiment to Search for Light Dark Matter at the SPS,” arXiv:1312.3309 [hep-ex].
 - [21] Y. S. Tsai, “Axion Bremsstrahlung By An Electron Beam,” Phys. Rev. D **34**, 1326 (1986).
 - [22] See, for example, <http://sba.web.cern.ch/sba/>
 - [23] D. Banerjee, P. Crivelli and A. Rubbia, “Beam Purity for Light Dark Matter Search in Beam Dump Experiments,” Adv. High Energy Phys. **2015** (2015) 105730.
 - [24] B. Aubert *et al.* [BaBar Collaboration], “Search for Invisible Decays of a Light Scalar in Radiative Transitions $v_{3S} \rightarrow \gamma A_0$,” arXiv:0808.0017 [hep-ex].
 - [25] A. V. Artamonov *et al.* [BNL-E949 Collaboration], “Study of the decay $K^+ \rightarrow \pi^+ \nu \bar{\nu}$ in the momentum region $140 < P(\pi) < 199$ -MeV/c,” Phys. Rev. D **79** (2009) 092004.
 - [26] H. S. Lee, “Muon $g-2$ anomaly and dark leptonic gauge boson,” Phys. Rev. D **90** (2014) 9, 091702.
 - [27] G. A. Akopdzhanov *et al.*, “Determination of Photon Coordinates in Hodoscope Cherenkov Spectrometer,” Nucl. Instrum. Meth. **140** (1977) 441.
 - [28] V. A. Davydov, A. V. Inyakin, V. A. Kachanov, R. N. Krasnokutsky, Y. V. Mikhailov, Y. D. Prokoshkin and R. S. Shuvalov, “Particle Identification in Hodoscope Cherenkov Spectrometer,” Nucl. Instrum. Meth. **145** (1977) 267.